



# The Solar system's post-main-sequence escape boundary

Dimitri Veras<sup>★</sup> and Mark C. Wyatt

Institute of Astronomy, University of Cambridge, Madingley Road, Cambridge CB3 0HA

Accepted 2012 January 9. Received 2012 January 4; in original form 2011 December 2

## ABSTRACT

The Sun will eventually lose about half of its current mass non-linearly over several phases of post-main-sequence evolution. This mass loss will cause any surviving orbiting body to increase its semimajor axis and perhaps vary its eccentricity. Here, we use a range of solar models spanning plausible evolutionary sequences and assume isotropic mass loss to assess the possibility of escape from the Solar system. We find that the critical semimajor axis in the Solar system within which an orbiting body is guaranteed to remain bound to the dying Sun due to perturbations from stellar mass loss alone is  $\approx 10^3$ – $10^4$  au. The fate of objects near or beyond this critical semimajor axis, such as the Oort Cloud, outer scattered disc and specific bodies such as Sedna, will significantly depend on their locations along their orbits when the Sun turns off the main sequence. These results are applicable to any exoplanetary system containing a single star with a mass, metallicity and age which are approximately equal to the Sun's, and suggest that few extrasolar Oort Clouds could survive post-main-sequence evolution intact.

**Key words:** minor planets, asteroids: general – Oort Cloud – planets and satellites: dynamical evolution and stability – planet–star interactions – stars: AGB and post-AGB – stars: evolution.

## 1 INTRODUCTION

The fate of our Solar system is of intrinsic human interest. From the present day, the Sun will continue to exist in a main-sequence phase for at least 6 Gyr longer, and then experience post-main-sequence phases before ending its life as a white dwarf. The post-main-sequence phases will be violent: the Sun's radius and luminosity will likely vary by several orders of magnitude while the Sun ejects approximately half of its present-day mass through intense winds. The effect on orbiting bodies, including planets, asteroids, comets and dust, may be catastrophic.

The future evolution of the Solar system between now and the end of the Sun's main sequence will be largely unaffected by the solar mass loss. The Sun's current mass-loss rate lies in the range  $\sim 10^{-14}$  to  $10^{-13} M_{\odot} \text{ yr}^{-1}$  (e.g. Cohen 2011; Pitjeva & Pitjev 2012). As demonstrated by Veras et al. (2011), all orbiting objects would evolve adiabatically due to this small mass loss. Thus, assuming the mass-loss rate remains constant by the end of the main sequence, their eccentricities will remain unchanged, and their semimajor axes would increase by at most  $\approx 0.055$  per cent. The Sun's main-sequence mass-loss rate, has, however, varied over time. Wood et al. (2002) and Zendejas, Segura & Raga (2010) suggest that this mass-loss rate was orders of magnitude greater when the Sun began life on the main sequence, and is a monotonically decreasing function of time. Therefore, 0.055 per cent represents an upper bound. Re-

gardless, this potentially slight orbital expansion, uniformly applied to all orbiting objects, is not predicted to change the dynamics of the Solar system.

Instead, the primary driver of dynamical change in the Solar system during the Sun's main sequence will arise from the mutual secular perturbations of the orbiting bodies. Kholshevnikov & Kuznetsov (2007) provide a comprehensive review of the investigations up until the year 2007 which have contributed to our understanding of this evolution. These studies describe orbital evolution beyond  $10^4$  yr from now in a primarily *qualitative* manner because numerical integrations typically cannot retain the orbital phase information of the terrestrial planets over the Sun's main-sequence lifetime. Further, Mercury might suffer a close encounter with Venus (Laskar 2008), and the orbital motion of the other inner planets is predicted to be chaotic. The outer planets, however, are predicted to survive and harbour quasi-periodic motion. Since this review, additional studies have primarily focused on the complex evolution of the terrestrial planets; Laskar et al. (2011) helps affirm the intractability of terrestrial orbital phases over long times. Other studies (Batygin & Laughlin 2008 and Laskar 2008) corroborate previous results about how the outer Solar system planets (Jupiter, Saturn, Uranus and Neptune) should remain stable in near-circular ( $e < 0.1$ ) orbits, even though the orbits themselves may be chaotic (Hayes 2007, 2008; Hayes, Malykh & Danforth 2010).

This uncertainty of a planet's orbital architecture at the beginning of the Sun's post-main-sequence phases renders difficult the determination of the fate of individual presently known bodies. Regardless, several studies have explored the effect of the Sun's

<sup>★</sup>E-mail: veras@ast.cam.ac.uk

post-main-sequence evolution on the planets. The outcome for the Earth is controversial because investigators differ on whether the Earth's expanding orbit will 'outrun' the Sun's expanding envelope and on how to model the resulting tidal interactions (see Schröder & Connon Smith 2008, and references therein). Duncan & Lissauer (1998) consider the stability and orbits of Jupiter, Saturn, Uranus and Neptune with mass scalings and a post-main-sequence mass-loss prescription from Sackmann, Boothroyd & Kraemer (1993). They find that this prescription yields 'no large growth in planetary eccentricities', but mention the possibility of Oort Cloud comets being ejected during periods of brief, rapid mass loss. Complementary studies of other planetary systems have explored in more detail how Oort Cloud comet analogues may become unbound (Alcock, Fristrom & Siegelman 1986; Parrott & Alcock 1998).

Our study is devoted to exploring the prospects for dynamical ejection from the Solar system by using realistic multiphasic non-linear mass-loss prescriptions from the SSE code (Hurley, Pols & Tout 2000) and by treating isolated objects beyond the influence of any potentially surviving planets. We do so by using the analytical mass-loss techniques in Veras et al. (2011), which yield a critical semimajor axis,  $a_{\text{crit}}$ , within which an orbiting object is guaranteed to remain bound. In Section 2, we present the solar evolutionary models used, highlighting those which are later applied to  $N$ -body simulations that help reaffirm the validity of  $a_{\text{crit}}$ . In Section 3, we define  $a_{\text{crit}}$ , plot it as a function of solar evolution model and explore the properties of some representative orbits. In Section 4, we explore the implications for the scattered disc and the Oort Cloud. We discuss the results in Section 5 and conclude in Section 6.

## 2 SOLAR EVOLUTION MODELS

We utilize the SSE code (Hurley et al. 2000), which yields a complete stellar evolutionary track of a star for a given initial stellar mass, metallicity and mass-loss prescription. We denote the Sun's mass as  $M_*(t)$  and define a solar mass  $\equiv 1 M_\odot$  to be the *current value* of the Sun's mass. We assume that the Sun's current metallicity is  $[\text{Fe}/\text{H}]_\odot \equiv 0.02$ . We also assume that the Sun has already been evolving on the main sequence for exactly 4.6 Gyr.

The remaining, and unknown, constraint to include is the Sun's post-main-sequence mass loss. On the asymptotic giant branch (AGB), we use the mass-loss prescription from Vassiliadis & Wood (1993):

$$\log \frac{dM_*}{dt} = -11.4 + 0.0125 [P - 100 \max(M_* - 2.5, 0.0)], \quad (1)$$

such that  $dM_*/dt$  is computed in  $M_\odot \text{ yr}^{-1}$  and where

$$\log P \equiv \min(3.3, -2.07 - 0.9 \log M_* + 1.94 \log R_*), \quad (2)$$

where  $P$  is computed in years and  $R_*$  is the radius of the Sun.

On the red giant branch (RGB), mass loss is often modelled to have the following 'Reimers law' functional form (Kudritzki & Reimers 1978):

$$\frac{dM_*}{dt} = \eta (4 \times 10^{-13}) \frac{L_*(t) R_*(t)}{M_*} \frac{M_\odot}{\text{yr}}, \quad (3)$$

where  $L_*$  represents the solar luminosity and  $\eta$  is an important dimensionless coefficient whose magnitude helps determine the sequence of stellar evolutionary phases. Sackmann et al. (1993) compute evolutionary models for the Sun, and state that  $0.4 < \eta < 0.8$  represent 'reasonable mass-loss rates'. This conforms with the typically used value of  $\eta = 0.5$  (e.g. Kudritzki & Reimers 1978; Hurley et al. 2000; Bonsor & Wyatt 2010). An updated version

of the Reimers law (Schröder & Cuntz 2005) contains two new multiplicative factors:

$$\left( \frac{T_{\text{eff}}}{4000 \text{ K}} \right)^{3.5} \left[ 1 + \frac{g_\odot}{4300 g_*} \right], \quad (4)$$

where  $g_*$  and  $T_{\text{eff}}$  are the star's surface gravity and effective temperature, respectively, and  $g_\odot$  is the current value of the solar surface gravity. The product of both these additional factors is not far from unity. According to Schröder & Cuntz (2005), who used the RGBs and horizontal branches of two globular clusters with very different metallicities for calibration, their effective value of  $\eta$  in the original Reimers law would be about 0.5.

All these considerations dissuade us from selecting a single value of  $\eta_\odot$  and instead lead us to consider the entire range  $0.2 \leq \eta_\odot \leq 0.8$ ; we sample  $\eta_\odot$  values in this range in increments of 0.01. Representative evolutionary sequences in this range are displayed in the upper panel of Fig. 1. In all cases, the Sun undergoes a  $\gtrsim 0.5$  Gyr long transition towards the foot of the RGB after leaving the main sequence. The Sun moves on to the RGB before enduring

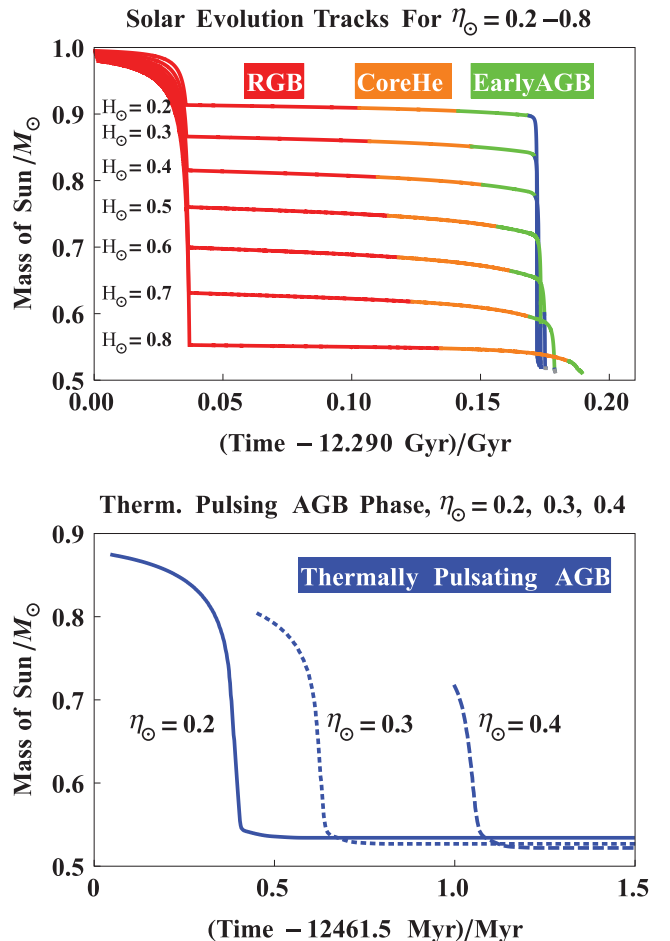


**Figure 1.** Potential solar evolutionary tracks. The upper panel displays at least a part of all phases from the RGB phase to the thermally pulsing AGB phase for seven representative values of  $\eta_\odot$  (the nearly flat RGB curves before 12.290 Gyr are not shown). The lower panel zooms in on and isolates the thermally pulsing AGB phase for  $\eta_\odot = 0.2$  (solid line),  $\eta_\odot = 0.3$  (dotted line) and  $\eta_\odot = 0.4$  (dashed line). Time is measured from the beginning of the Sun's main sequence. The plot demonstrates how the choice of  $\eta_\odot$  can drastically alter the percentage of solar mass lost and solar mass-loss rate per phase.

a period of core helium burning and subsequent evolution on the early AGB, as defined by Hurley et al. (2000). Then, for  $\eta_{\odot} \leq 0.74$ , the Sun will enter a thermally pulsing AGB phase before becoming a white dwarf. This intermediate phase is bypassed for  $0.75 \leq \eta_{\odot} \leq 0.80$ .

The different evolutionary sequences demonstrate that the greatest amount of mass lost and the greatest mass loss rate may occur during the RGB, early AGB or thermally pulsing AGB phases. In all cases, the total percentage of the Sun's current mass which is lost is  $\approx 46.5$ – $49.0$  per cent. The value of  $\eta$  determines how much envelope mass is lost on the RGB, and hence, the amount of envelope mass which remains at the start of the AGB. For  $\eta_{\odot} \lesssim 0.5$ , most of this disposable mass is reserved for the AGB, whereas for  $\eta_{\odot} \gtrsim 0.5$ , most of this mass is lost during the RGB phase. When  $\eta$  is large enough ( $\eta_{\odot} \geq 0.75$ ), enough of the envelope mass is lost during the RGB to cause the Sun to bypass the thermally pulsing AGB phase. In the extreme case of  $\eta_{\odot} \geq 0.94$  (not modelled here), the Sun would bypass helium burning and the AGB phases entirely, and would transition to a pure helium white dwarf directly from the RGB phase.

The lower panel zooms in and isolates the thermally pulsing AGB phase for  $\eta_{\odot} = 0.2$ – $0.4$ , where the mass-loss rate is greatest. Note that the time-scale for this mass loss is  $\approx 0.1$ – $0.3$  Myr, orders of magnitude shorter than the mass loss on the RGB.

### 3 THE CRITICAL SEMIMAJOR AXIS

#### 3.1 Equations

A star which is expunging mass beyond an orbiting object will cause the latter's orbit to expand. If the mass loss is large enough during one orbital period, then deformation of the orbit can cause the object to escape the system. We quantify these claims by defining a dimensionless 'mass-loss index' (Veras et al. 2011):

$$\Psi \equiv \frac{\text{mass loss time-scale}}{\text{orbital time-scale}} = \frac{\alpha}{n\mu}$$

$$= \frac{1}{2\pi} \left( \frac{\alpha}{1 M_{\odot} \text{ yr}^{-1}} \right) \left( \frac{a}{1 \text{ au}} \right)^{3/2} \left( \frac{\mu}{1 M_{\odot}} \right)^{-3/2}, \quad (5)$$

where  $\alpha$  represents the solar mass-loss rate,  $a$  and  $n$  represent the orbiting object's semimajor axis and mean motion, and  $\mu = M_{\star} + M_s$ , where  $M_s$  represents the mass of the object. We can assume  $\mu \approx M_{\star}$  because every known object which orbits the Sun has a mass that is  $< 0.1$  per cent of  $1 M_{\odot}$ . However, observations cannot yet exclude the possibility of the existence of a Jovian planet orbiting at a distance of at least several thousand au (Iorio 2011). Therefore, 'undiscovered' planets beyond  $\sim 10^4$  au might be massive enough to make a non-negligible contribution to  $\mu$ . Even if such a planet formed within the orbit of Neptune, gravitational scattering could have placed the planet in its present location (Veras, Crepp & Ford 2009). Alternatively, the planet could have previously been free-floating and subsequently captured by the Solar system.

Dynamical evolution critically depends on  $\Psi$ . When  $\Psi \ll 1$ , the orbiting object evolves 'adiabatically' such that  $a$  increases but its eccentricity,  $e$ , remains constant. Examples of objects with  $\Psi \ll 1$  include all eight of the inner and outer planets, both currently (see Section 1) and during any plausible post-main-sequence solar evolution phase. Alternatively, when  $\Psi \gg 1$ , in the 'runaway' regime,  $a$  continues to increase, but now  $e$  may achieve any value from zero to unity. Veras et al. (2011) demonstrate that the bifurcation point beyond which the motion is no longer adiabatic is not sharp

and occurs at  $\Psi_{\text{bif}} \sim 0.1$ – $1.0$ . In fact, if  $\Psi$  is instead defined as  $\alpha T / \mu$ , where  $T$  is the orbital period of the orbiting object, then this definition differs from equation (5) by a factor of  $1/(2\pi) \approx 0.16$ . Therefore, both definitions effectively bound the approximate location of the bifurcation point when  $\Psi = 1$ , and we consider both possibilities in our analysis.

The Sun loses mass non-linearly, as showcased in Fig. 1. One can apply the analytical linear results from Veras et al. (2011) to a non-linear mass-loss profile by partitioning the profile into  $N$  smaller approximately linear stages, with mass-loss rates of  $\alpha_1, \alpha_2, \dots, \alpha_i, \dots, \alpha_N$ , as in Veras & Tout (2012). If all these segments occur in the adiabatic regime, then we can relate the semimajor axis and eccentricity at the start of the first segment to these same elements at the end of segment  $i$ , with

$$a_i = a_0 \left( \frac{\mu_i}{\mu_0} \right)^{-1} \equiv a_0 \beta_i^{-1}, \quad (6)$$

$$e_i = e_0. \quad (7)$$

Because the orbiting object's eccentricity does not change in this regime, the body will remain bound in the absence of additional perturbations.

All orbiting bodies will be expanding their semimajor axis at the same rate. The mass-loss index at the end of segment  $i$  will be

$$\Psi_i = \kappa \alpha_i \left( \frac{a_0 \mu_0}{\mu_i^2} \right)^{3/2}, \quad (8)$$

where  $\kappa = 1$  or  $2\pi$ , depending on whether  $\Psi$  is defined with respect to the mean motion (equation 5) or the orbital period.  $\kappa$  could also be treated generally as a tunable parameter which may better pinpoint the location of the bifurcation point in specific cases. The first instance at which the orbiting object *may* escape is when the evolution becomes non-adiabatic, and hence the eccentricity can vary. This occurs when  $\Psi_i \approx 1$ . Therefore, the minimum percentage of  $\mu_0$  which must be retained in order to guarantee that the orbiting object will remain bound in a given segment  $i$  is

$$\beta_{\text{crit}_i} \equiv \left( \frac{\mu_i}{\mu_0} \right)_{\text{crit}}^{1/3} \approx \kappa^{1/3} \left( \frac{\alpha_i}{1 M_{\odot} \text{ yr}^{-1}} \right)^{1/3} \left( \frac{a_0}{1 \text{ au}} \right)^{1/2} \left( \frac{\mu_0}{1 M_{\odot}} \right)^{-1/2}. \quad (9)$$

Hence, the critical  $a_0$ , termed  $a_{\text{crit}}$ , at which an orbiting object will remain in the adiabatic regime, and thus bound to a  $1 M_{\odot}$  star, is

$$\frac{a_{\text{crit}}}{1 \text{ au}} \approx \kappa^{-2/3} \min \left[ \beta_i^2 \left( \frac{\alpha_i}{1 M_{\odot} \text{ yr}^{-1}} \right)^{-2/3} \right], \quad (10)$$

where the minimum is taken over all segments  $i$ .

#### 3.2 Mass-loss profile partition

The accuracy of  $a_{\text{crit}}$  depends on how finely the solar mass-loss profile is partitioned into stages. Given the focused nature of our study, we simply adopt the most accurate option by treating each SSE timestep as a segment. These segments also include transitions between evolutionary phases, for which a mass loss and time-scale is computed by SSE in every case. We choose output parameters which yield 3333 outputs total per simulation for the RGB, core helium burning, early AGB and thermally pulsing AGB phases, and at least 20 outputs for each of the other phases of evolution. Our choices are motivated by the observation that the segment which satisfies

equation (10) always arises from the RGB or an AGB phase. The minimum SSE timesteps are  $\approx 10^3$  yr long, which is shorter than the orbital period of the objects we consider here. Equation (10) is valid for any relation between SSE timesteps and orbital period because, in the adiabatic regime, the semimajor axis and eccentricity evolution is independent of the location of the object along its orbit. We apply this output parametrization uniformly across the  $\eta_{\odot}$  values sampled.

### 3.3 N-body simulations

We supplement the computation of  $a_{\text{crit}}$  (from the stellar evolution profiles alone) with  $N$ -body simulations of orbiting objects. These simulations help affirm that objects with  $a < a_{\text{crit}}$  do remain bound, and provide a rough characterization of the motion of objects which are susceptible to escape. We select the seven solar evolutionary pathways corresponding to  $\eta_{\odot} = [0.2, 0.3, 0.4, 0.5, 0.6, 0.7, 0.8]$  for these simulations, and use a second-order mixed-variable symplectic integrator from a modified version of the MERCURY integration package (Chambers 1999). All orbiting objects are treated as test particles for computational ease and so that they could be integrated simultaneously. Because  $\mu$  is dominated by  $M_{\star}$ , an isolated giant planet would react to stellar mass loss nearly equivalently to an isolated test particle on the same orbit. After each MERCURY timestep, we linearly interpolate the value of the Sun's mass from the SSE output. This approximation is sufficient for numerical integrations which do not feature close encounters.

Simulating orbital evolution throughout the remaining lifetime of the Solar system with numerical integrations and without utilizing secular approximations is computationally unfeasible and, for this project, unnecessary. Our focus is on the behaviour of objects when they are most susceptible to escape. Therefore, having already identified when the greatest mass loss occurs, we simulate the entire thermally pulsating AGB phase for the  $\eta_{\odot} = [0.2, 0.3, 0.4]$  simulations (see Fig. 1). The duration of these simulations is between  $2.7 \times 10^5$  and  $5.7 \times 10^5$  yr. For  $\eta_{\odot} = [0.5, 0.6, 0.7, 0.8]$ , we simulate solar mass evolution from when  $M_{\star} = 0.98000 M_{\odot}$ , which occurs during the RGB, until the beginning of the white dwarf phase (see Fig. 1). For these simulations, modelling the phases after the RGB may be important because despite their overall low mass-loss rates, the AGB phases could feature short bursts of high mass loss. Also,  $\beta_i$  is lower for the phases beyond the RGB. The duration of these simulations is between  $1.64 \times 10^8$  and  $1.88 \times 10^8$  yr.

We choose the initial conditions for the orbiting objects as follows. The orbital evolution of an orbiting object which is susceptible to escape is highly dependent on  $e$  and its true anomaly  $f$  (see Veras et al. 2011). For linear mass loss and  $\Psi \gg 1$ , the object's eccentricity is likely to initially increase. However, the eccentricity must initially decrease if  $f_{\text{crit}} \leq f \leq (360^\circ - f_{\text{crit}})$ , where  $f_{\text{crit}} = 180^\circ - (1/2)\cos^{-1}(7/9) \approx 160^\circ$ , and we wish to sufficiently sample this behaviour as well. These considerations motivate us to choose  $f_0$  in increments of  $30^\circ$  from  $0^\circ$  to  $330^\circ$ , supplemented by  $f_0 = [160^\circ, 170^\circ, 190^\circ, 200^\circ]$ . In order to sample a wide range of eccentricities, we choose  $e_0 = [0.0, 0.2, 0.4, 0.6, 0.8, 0.95]$ . Because application of equation (10) demonstrates that  $10^3$  au  $\lesssim a_{\text{crit}} \lesssim 10^4$  au, we choose  $a_0/\text{au} = [10^2, 10^3, 3 \times 10^3, 5 \times 10^3, 10^4, 10^5]$ . The smallest of these values yields a period of 414 yr for  $M_{\star} = 0.5 M_{\odot}$ . Therefore, we choose a timestep less than 1/50th of this value,  $1 \times 10^4$  d, for all our numerical simulations. Because this timestep might not sample the pericentre sufficiently for highly eccentric orbits, we perform an identical set of simulations with a timestep which is one order of magnitude lower as a check on the results.

### 3.4 Visualizing the critical semimajor axis

We plot  $a_{\text{crit}}$  from equation (10) assuming  $\kappa = 1$  as a function of  $\eta_{\odot}$  in Fig. 2. The curve illustrates that for  $\eta_{\odot} \leq 0.5$ ,  $a_{\text{crit}} \approx 10^3$  au, and for  $\eta_{\odot} = 0.7$ ,  $a_{\text{crit}} \approx 10^4$  au. Other values of  $a_{\text{crit}}$  lie in between these two extremes. The curve is coloured according to the stellar evolutionary phase at which an orbiting object is most susceptible to ejection, which depends on a combination of the mass-loss rate and the mass remaining in the Sun. Three different phases (red = RGB, green = early AGB and blue = thermally pulsing AGB) are represented on the curve, demonstrating the sensitivity of  $a_{\text{crit}}$  to the stellar model chosen. When the RGB evolution dominates the orbiting object's motion, the critical semimajor axis is higher than in the AGB-dominated cases because RGB evolution takes place earlier in the Sun's post-main-sequence life, when the Sun has more mass. Any objects in the pink shaded region above the curve might escape; those in the white region below the curve are guaranteed to remain bound.

The overlaid symbols indicate the results of the  $N$ -body simulations. Check marks indicate that every orbiting object from every  $\{e_0, f_0\}$  bin sampled remained bound ( $e < 1$ ) for the duration of the simulation. Crosses indicate that at least one orbiting object becomes unbound, either through the orbit becoming hyperbolic ( $e > 1$ ) or through the body achieving  $a \gtrsim 10^6$  au. The number of crosses indicate the number of  $e_0$  bins in which at least one orbiting object became unbound. The  $N$ -body simulations help affirm that all of the objects below the curve remained bound. This also holds true if  $\kappa = 2\pi$ . In that case, the curve would keep the same form but be lowered by a factor of  $(2\pi)^{2/3} \approx 3.4$ . This value of  $\kappa$  would provide a more conservative estimate for the Solar system's critical semimajor axis and would still ensure that any known surviving planets and belts would remain bound. Objects with high values of  $e_0$  are usually, but not always, prone to escape; additional cross symbols suggest that objects escaped at progressively lower values of  $e_0$ . The number of crosses displayed does not show uniform patterns primarily because of the complex dependencies of the evolution in the adiabatic/runaway transitional regime on  $a$ ,  $e$  and  $f$  (see Section 4.2). Also, the parameter space sampled is limited and the  $N$ -body simulations do not model the entire pre-white-dwarf lifetime of the Sun.

Not shown in Fig. 2 are the results from the  $a_0 = 10^2$  and  $10^5$  au simulations. In the former, every orbiting object remains bound (corresponding to a row of check marks). In the latter, at least one orbiting object escapes for each value of  $\eta_{\odot}$  integrated (corresponding to a row of different numbers of crosses).

### 3.5 Properties of the critical stage

Here we take a closer look at the critical stage which yields  $a_{\text{crit}}$  through Figs 3–6. Figs 3–4 demonstrate that the critical stage occurs nearly at the end of the Sun's post-main-sequence life, when the Sun will have already lost the majority of its disposable mass. The solid black curve in Fig. 3 is a poor proxy of the  $a_{\text{crit}}$  curve from Fig. 2. Both Figs 3 and 4 suggest that  $\eta_{\odot} = 0.7$  represents a bifurcation point in solar evolution, which is approximately where the thermally pulsing AGB stage becomes transitory. The critical time from the start of the Sun's main sequence will be  $\approx 12.465 \pm 0.005$  Gyr for  $\eta_{\odot} \leq 0.7$  and  $12.326 \pm 0.0002$  Gyr for  $\eta_{\odot} \geq 0.7$ . These are remarkably well-constrained values relative to the curves in Fig. 2.

Now consider  $\alpha_i$  at the critical stage. Fig. 5 shows that this mass-loss rate varies between  $\approx 2 \times 10^{-7}$  and  $\approx 5 \times 10^{-6} M_{\odot} \text{ yr}^{-1}$ . Also, this rate closely mirrors the maximum rate achieved throughout the

## The Solar System's Stability Boundary

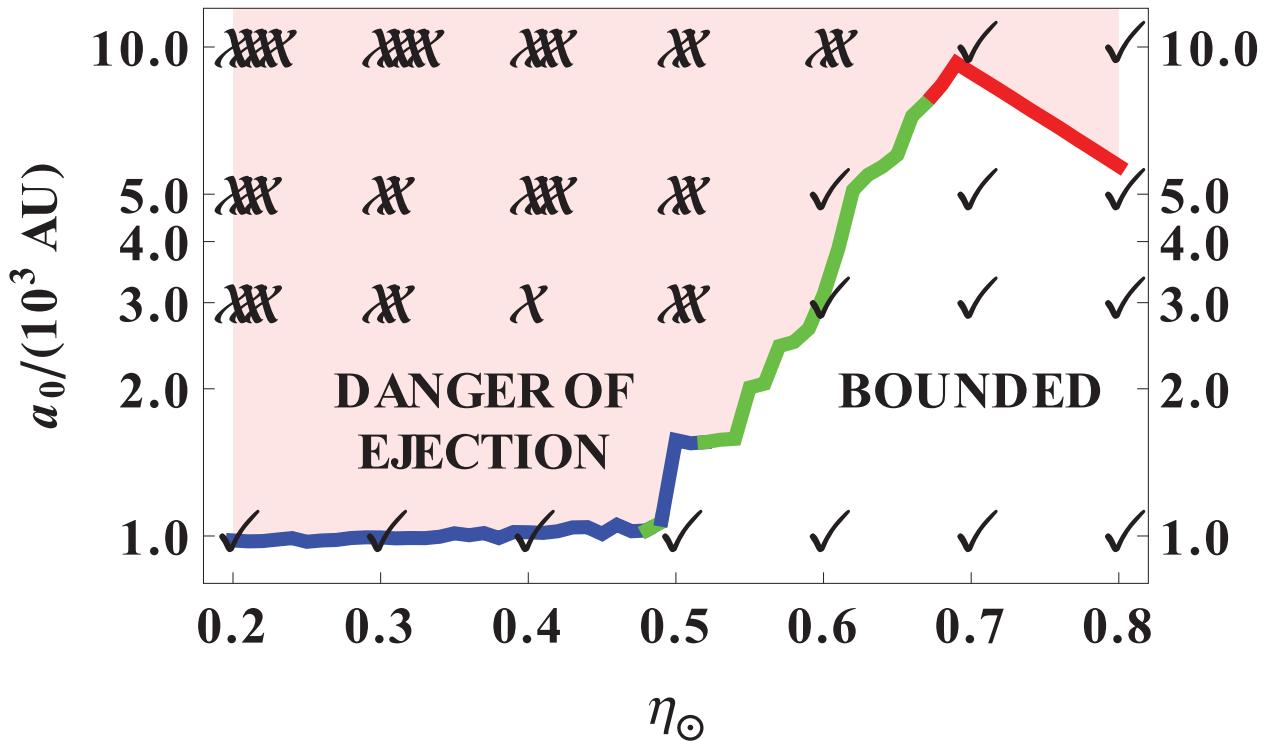


**Figure 2.** The Solar system's critical semimajor axis, as a function of the solar Reimers mass loss coefficient,  $\eta_\odot$ . The curve is derived from equation (10). In the shaded pink region above the curve, orbiting bodies may escape the dying Sun on hyperbolic orbits. In the white region below the curve, bodies are guaranteed to remain bound on elliptical orbits. The colour of the line segments indicates the solar phase in which orbiting bodies are most susceptible to escape: red = RGB, green = early AGB and blue = thermally pulsing AGB. Check marks and crosses provide information about the results of  $N$ -body integrations (see Section 3.3). Check marks indicate that every orbiting object in every  $N$ -body simulation remained bound. Each cross represents a different initial eccentricity value (out of the set  $\{0.0, 0.2, 0.4, 0.6, 0.8, 0.95\}$ ) of at least one body which escaped. An alternate curve, with  $\kappa = 2\pi$ , would have the same form but with values which are  $(2\pi)^{2/3} \approx 3.4$  times lower than the ones shown here, yielding a more conservative estimate. This plot demonstrates that Solar system bodies must satisfy  $a < 10^3$  au when the Sun turns off the main sequence in order to be guaranteed protection from escape.

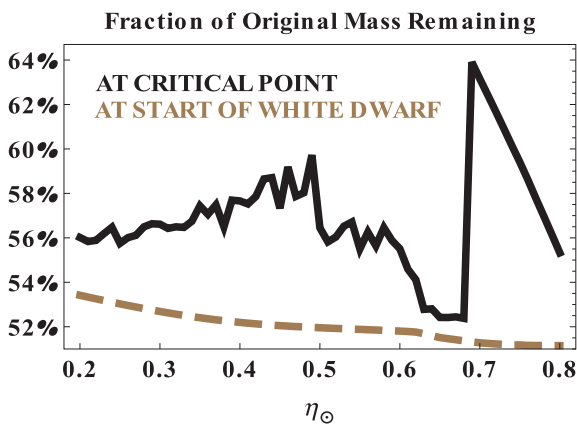


**Figure 3.** The percentage of  $1 M_\odot$  remaining in the Sun at the moment when orbiting bodies are most likely to escape (solid black curve) and at the moment the Sun becomes a white dwarf (dashed brown curve). Orbiting bodies are most likely to escape the Solar system after the Sun has lost at least  $0.35 M_\odot$ .

simulation, given by the dashed brown curve. Therefore, by itself,  $\max(\alpha_i)$  is an excellent indicator of the stability prospects of an orbiting body. Also, this trend suggests that short violent outbursts from planet-hosting stars can jeopardize the survival of orbiting

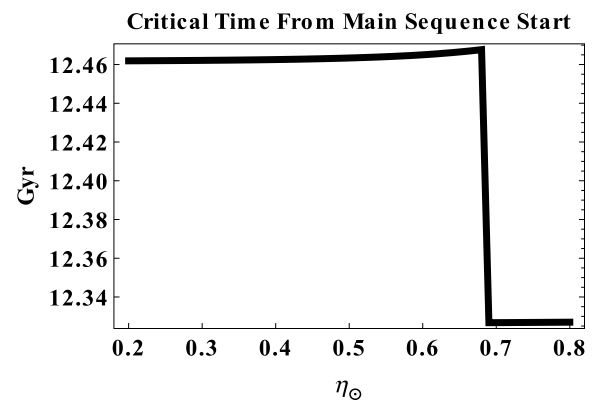


**Figure 4.** The time from the start of the Sun's main sequence that orbiting bodies are most likely to escape the Solar system. Despite the complex variance in solar evolution as a function of  $\eta_\odot$ , this critical time has a relatively smooth, piecewise dependence on  $M_\odot$ .

bodies. The Solar system is subject to the same danger even though the Sun is not expected to experience a violent outburst with  $\alpha > 5 \times 10^{-6} M_\odot \text{ yr}^{-1}$  from these models. If we are underestimating the variability of the Sun after it turns off the main sequence, then orbiting bodies can be in greater danger of escape than we currently expect.

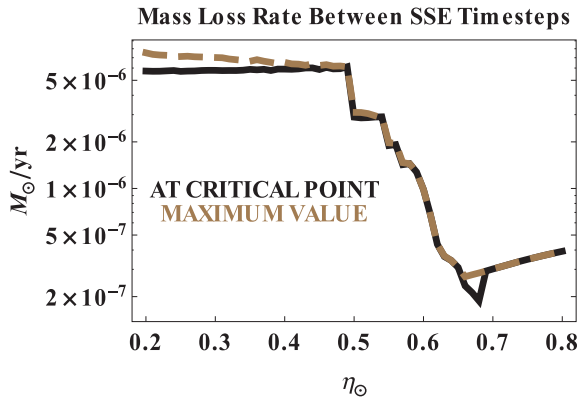


**Figure 5.** The mass-loss rate at the moment when orbiting bodies are most likely to escape (solid black curve) and when this value takes on a maximum (dashed brown curve). The excellent agreement between the two curves suggests that mass-loss rate alone, regardless of the amount of mass remaining in the Sun, is the primary indicator of when an orbiting body is no longer safe from ejection.

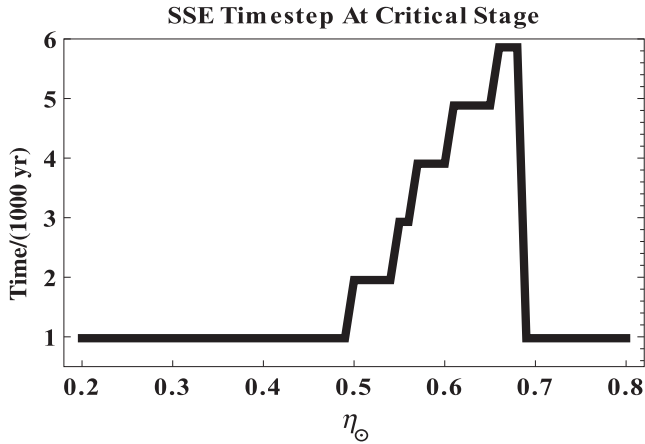


**Figure 6.** The SSE timestep at the moment when orbiting bodies are most likely to escape. Although short on the time-scale of Solar system evolution, this timestep is long relative to a solar rotation period, where additional variability which is not modelled here might occur. The mass loss over this timestep is treated as linear.

If such variability is on a time-scale which is shorter than the timesteps used in these simulations, then  $a_{\text{crit}}$  is being overestimated. Fig. 6 illustrates the timestep from which the mass-loss rate at the critical stage was computed. In all cases, this timestep is between  $\sim 980$  and  $5860$  yr. The Sun's current rotational period is less than one month; during a single rotation, prominences may erupt and sunspots may appear, among other phenomena. The Sun's (unknown) post-main-sequence variability will likely be more violent, but on a similar time-scale. If so, then short bursts of intense mass loss could be important but are not modelled by the comparatively long SSE timesteps.

### 3.6 Orbital properties

#### 3.6.1 Overview

Here we analyse some representative orbits from the  $N$ -body simulations. Because the time-scale for mass loss from the bottom panel of Fig. 1 is orders of magnitude shorter than the top panel, the difference in orbital properties is pronounced. Specifically, for  $a_0 >$

$10^3$  au and  $\eta_{\odot} < 0.5$ , all eccentricity variations will often occur during a single orbit. Alternatively, for  $\eta_{\odot} \geq 0.5$ , these variations occur over many orbits. We consider one case from the former category and two cases from the latter in detail. Additionally, we consider the eccentricity evolution for one case in the runaway regime, with  $a_0 = 10^5$  au and  $\eta_{\odot} = 0.2$ , and demonstrate here that objects near their apocentres do remain bound in this case, as predicted by the linear theory.

#### 3.6.2 Example bounded orbits for $\eta_{\odot} < 0.5$

We consider here short orbits ( $a_0 = 3 \times 10^3$  au) which are significantly disrupted by mass loss that takes place entirely within an orbital period ( $\eta_{\odot} = 0.3$ , see Fig. 1) and remain ellipses. Fig. 7 illustrates the orbital evolution of 16 objects, all with different  $f_0$  values, which all begin the  $N$ -body simulation with small-eccentricity ( $e_0 = 0.2$ ) orbits. These objects may be treated as low-eccentricity, inner Oort Cloud bodies. Despite the small  $e_0$ , the semimajor axes all increase by a factor of  $\approx 1.5$ – $2.2$ , and the final values of  $e$  range from  $\approx 0.1$  to  $0.6$ . If this mass was lost adiabatically, then the semimajor axis would increase by a factor of  $\approx 1.5$ , the lower bound of the actual increase in  $a$ . Further, the  $f_0 = 240^\circ$  object (brown curves) becomes nearly circularized at  $t \approx 12461.67$  Myr; if mass loss ceased at this point, then the body would maintain this nearly circular orbit.

Mass loss has a dramatic effect on the evolution of  $f$ . A system no longer is adiabatic when  $df/dt = 0$  (Veras et al. 2011). At this point,  $f$  stops circulating and begins to librate. The lower left plot illustrates how the mass loss slows  $df/dt$  for each orbiting object. Although none of the orbiting objects achieves  $df/dt = 0$ , the  $f_0 = 90^\circ$  object (black curves) comes closest. This is also the object whose  $a$  and  $e$  values are increased by the greatest amount. Alternatively, the highest ending value of  $df/dt$  is associated with the  $f_0 = 240^\circ$  object, whose eccentricity decreases the most. In the linear mass-loss approximation, for  $\Psi \gg 1$ , bodies closest to pericentre are most susceptible to escape. This plot helps demonstrate how no such correlation exists if the evolving regime is not runaway.

Although the bottom-right plot might suggest that some planets appear to be leaving this system, all bodies will remain bound, orbiting the solar white dwarf with their values of  $a$  and  $e$  attained at  $t = 12461.9$  Myr, assuming no additional perturbations.

#### 3.6.3 Example escape orbits for $\eta_{\odot} \geq 0.5$

Here we consider longer orbits ( $a_0 = 1 \times 10^4$  au) which are significantly disrupted by mass loss that takes place over several orbital periods ( $\eta_{\odot} = 0.5, 0.6$ ; see Fig. 1) and which can cause an orbiting object to escape. We consider highly eccentric orbits ( $e_0 = 0.8$ ) and compare two types of escape in Fig. 8: the left-hand panels showcase the  $f_0 = 0^\circ$  (red) object achieving an orbit with  $e = 0.99872$  and  $a > 10^6$  au (two orders of magnitude higher than  $a_0$ ), while the right-hand panels showcase the  $f_0 = 160^\circ$  (pink) object achieving a hyperbolic orbit. The only initial parameter changed in the two plot columns was the value of  $\eta_{\odot}$  (0.5 on the left and 0.6 on the right).

As evidenced by the plots in the upper two rows, the first strong burst of mass loss at  $t \approx 12.22$  Gyr provides a stronger orbital kick for  $\eta_{\odot} = 0.6$  solar evolution. However, as indicated by Fig. 2, the second, stronger burst of mass loss at  $t \approx 12.36$  Gyr yields a lower value of  $a_{\text{crit}}$  for  $\eta_{\odot} = 0.5$ . Regardless, this second strong burst of mass loss for both  $\eta_{\odot}$  values is roughly comparable, as the final range of  $a$  and  $e$  values are similar.

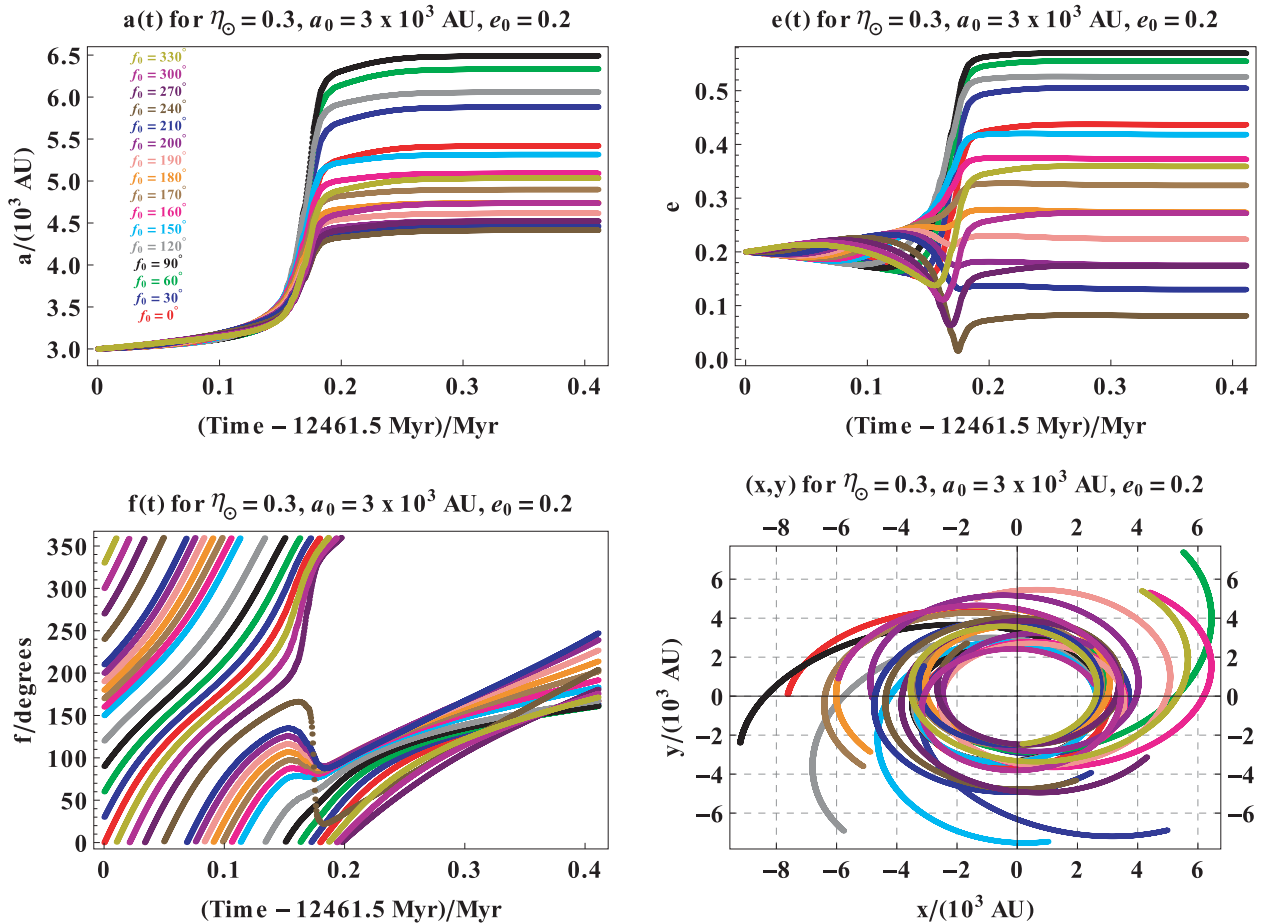


**Figure 7.** The orbital evolution of objects at  $a_0 = 3 \times 10^3 \text{ au}$  with  $e_0 = 0.2$  from 12 461.5 Myr. All of these bodies remain bound to the dying Sun, despite sometimes severe disruption to their orbits; the double cross in Fig. 2 corresponding to this initial pair ( $a_0, \eta_\odot$ ) indicates that escape occurred for  $e_0 \geq 0.8$ . The lower-right plot demonstrates that the disruption occurs within a single orbital period, and can stretch or contract orbits (upper-right plot) while widening them (upper-left plot). After this moment in time, the orbits assume osculating unchanging ellipses and remain on these orbits as the Sun becomes a white dwarf. The lower-left plot indicates that all objects barely remain in the adiabatic regime because  $df(t)/dt \neq 0$  for all cases at all times, ensuring that  $f$  continues to circulate, albeit slowly. The orbit which is most severely disrupted ( $f_0 = 90^\circ$ , black curve) comes closest to achieving  $df(t)/dt = 0$ .

The difference is enough, however, to cause escape in two different ways, one with an object which was at pericentre at the beginning of the simulation and one with an object which was near apocentre. This figure provides further confirmation of the difficulty, with correlating  $f_0$  with  $f$  for objects evolving in the transitional regime between the adiabatic and runaway regimes. Both  $f$  versus  $t$  plots demonstrate the expected change of behaviour during the second strong mass-loss event. However, they fail to distinguish between both types of escape, and neither technically reaches  $df/dt = 0$ . However, for the left- and right-hand panels, respectively,  $df/dt = 0.068$  and  $0.078 \text{ Myr}^{-1}$  at  $t = 12 461.9 \text{ Myr}$ .

The bottom panels show the spatial orbits of the objects; the left-hand panel illustrates all 16, and the right-hand panel features only four (for added clarity), including the escaping object. Due to the number of simulation outputs, lines are not connected between the output points. These plots explicitly illustrate how two bursts of mass loss from the Sun cause two distinct orbit expansions. Additionally, the apparent ‘noise’ about the equilibrium orbits attained before the second mass-loss event demonstrates the gradual expansion of the orbit due to minor mass-loss events. Comparing the colours and positions of both plots shows almost no correla-

tion with the identical initial conditions. The escaping pink body on the right-hand panel never reaches a distance to the Sun which is closer than its initial pericentre value (2000 au); the two dots for which  $x > 1.5 \times 10^4 \text{ au}$  indicate the path along which the body escapes.

### 3.6.4 Example orbits for rampant escape

We now consider objects in considerable danger of escape. These *can* reside at typical Oort Cloud distances,  $a_0 \sim 10^5 \text{ au}$ . The strong mass loss from the  $\eta_\odot = 0.2$  evolutionary track (with maximum  $\alpha \approx 7.5 \times 10^{-6} M_\odot \text{ yr}^{-1}$ ; see Fig. 5) yields  $\Psi \gtrsim 30 \gg 1$  and places these objects in the runaway regime. Here we determine if, unlike in the adiabatic regime, we can link the fate of an object with  $f_0$  amidst non-linear mass loss.

Fig. 9 confirms that we can. The results agree well with the linear theory. At the highest eccentricities sampled ( $e_0 = 0.95$ ), the objects initially at apocentre (orange;  $f_0 = 180^\circ$ ) remain bound to the dying Sun, and, further, suffer the greatest eccentricity decrease. Additionally, four other objects nearest to the apocentre of their orbits also remain bound. As the initial eccentricity of the

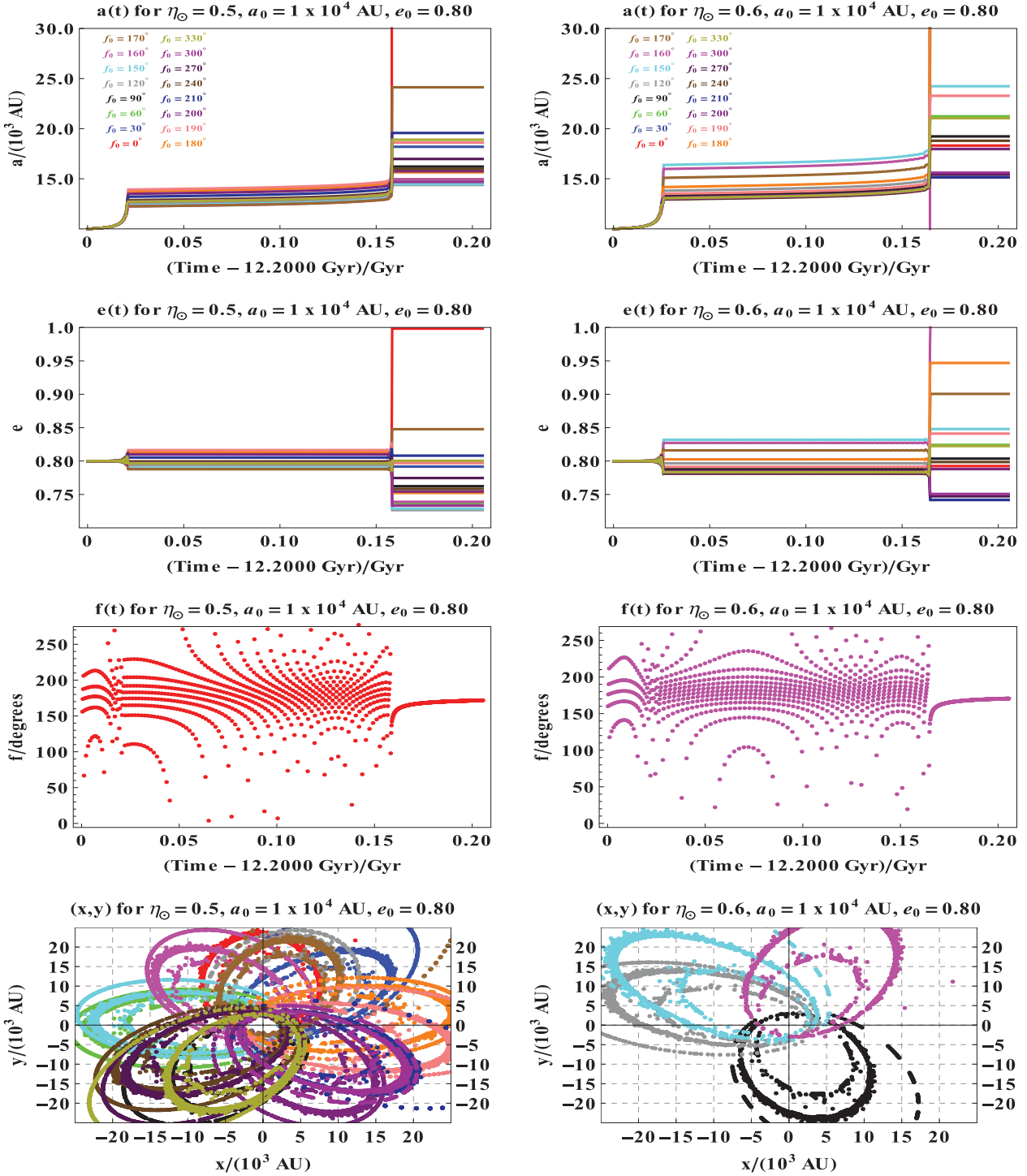


**Figure 8.** The orbital evolution of objects at  $a_0 = 1 \times 10^4$  au with  $e_0 = 0.8$  for  $\eta_{\odot} = 0.5$  (left-hand panels) and  $\eta_{\odot} = 0.6$  (right-hand panels) from 12.2 Gyr. In the left-hand panels, the  $f_0 = 0^\circ$  (red) body escapes when, after achieving  $e = 0.99872$ , its semimajor axis exceeds  $10^6$  au. Alternatively, in the right-hand panels, the  $f_0 = 160^\circ$  (pink) body escapes by achieving a hyperbolic orbit ( $e > 1, a < 0$ ). The  $f$  versus  $t$  panels demonstrate that the true anomaly cannot distinguish between these two types of escape in this case and that bodies may escape just before achieving  $df(t)/dt = 0$ . The pericentric versus near-apocentric  $f_0$  values of the escaping bodies, as well as a comparison of the orbital locations in the bottom two plots, indicate that the phase information is easily lost on the approach to  $df(t)/dt = 0$ . The bottom plots also demonstrate how the orbital architecture changes over several orbital periods, in contrast to Fig. 7. Note that the ejected planet in the bottom-right plot never comes within its initial pericentre value (2000 au) of the Sun.

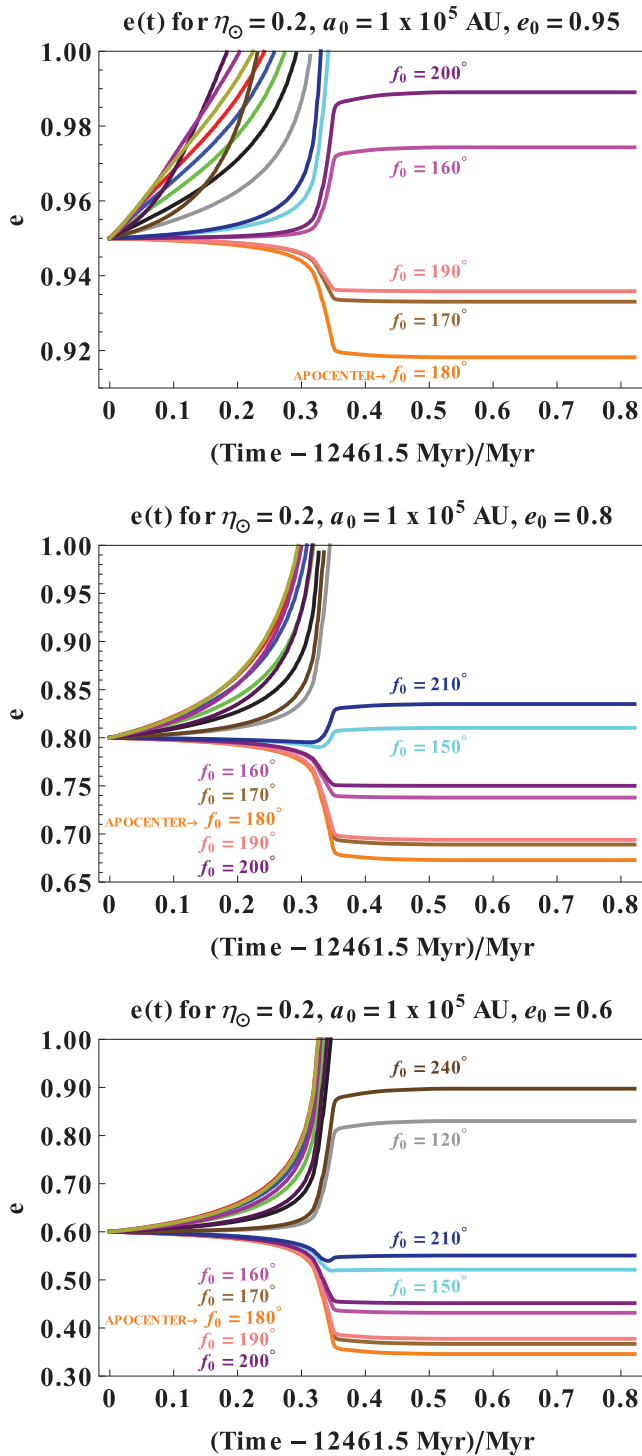


**Figure 9.** Eccentricity evolution in the runaway regime for typical Oort Cloud distances of  $10^5$  au and  $\eta_{\odot} = 0.2$ . Objects initially closest to the apocentre of their orbit are the most likely to survive, and bodies at their apocentres experience the largest net drop in eccentricity. Objects further away from the apocentre may survive if their initial eccentricity is decreased (from 0.95 in the top panel to 0.6 in the bottom panel).

objects is decreased (from 0.95 in the top panel to 0.6 in the bottom panel), more bodies which are increasingly further away from their initial apocentre are allowed to survive. Also, as the initial eccentricity is decreased, more bodies which are progressively further away from their initial apocentre suffer a net eccentricity decrease.

Note finally that the results are not symmetric about  $f_0 = 180^\circ$ : objects approaching apocentre are slightly more protected than objects leaving apocentre.

#### 4 APPLICATION TO THE SCATTERED DISC, OORT CLOUD AND OTHER TRANS-NEPTUNIAN OBJECTS

##### 4.1 Overview

The Solar system architecture beyond the Kuiper Belt is often divided into two distinct regions: the scattered disc and the Oort Cloud. The former is possibly an ancient, eroding remnant of Solar system formation, whereas the latter is thought to dynamically interact with the local Galactic environment and is continuously depleted and replenished. Both regions may supply each other with mass throughout the lifetime of the Solar system.

However, the definitions of these regions are not standardized. The boundary of the scattered disc is empirical and refers to objects with perihelia beyond Neptune ( $q > 30$  au) and semimajor axes beyond the 2:1 resonance with Neptune ( $a > 50$  au) (Luu et al. 1997; Gomes et al. 2008). Other papers have set a variety of numerical bounds based on their empirical readings of the semimajor axis–eccentricity phase space for objects beyond Neptune. In an early study, Duncan & Levison (1997) distinguished the Kuiper Belt from a scattered disc of objects with  $q \approx 32$ –48 au,  $e \leq 0.8$  and  $i \leq 50^\circ$ . Alternatively, sometimes the scattered disc is considered to be a subclass of the Kuiper Belt (e.g. Gladman & Chan 2006) and contains objects which satisfy the simpler constraint  $q \gtrsim 33$  au (Tiscareno & Malhotra 2003; Volk & Malhotra 2008) and  $e \gtrsim 0.34$  (Volk & Malhotra 2008), whereas Kaib & Quinn (2008) give  $q \geq 40$  au and Sheppard (2010) claim  $q \sim 25$ –35 au as the criterion for inclusion. Further, Levison, Morbidelli & Dones (2004) demonstrate how the scattered disc population has changed with time. For example, at an age of  $10^6$  yr, most scattered disc objects had  $q < 10$  au. More generally, Levison et al. (2008) define the currently observed scattered disc to be composed of objects with perihelia close enough to Neptune's orbit to become unstable over the (presumably main-sequence) age of the Solar system. However, some scattered disc objects may not be primordial, and instead represent a small transient population supplied by the Kuiper Belt. Also, because scattered disc objects interact with Neptune, some are depleted and diffused into the Oort Cloud.

If the scattered disc is insufficiently replenished from the Oort Cloud and Kuiper Belt, then the scattered disc may be depleted relative to its current level by the end of the Sun's main sequence. Whatever disc objects which might remain will continue to interact with Neptune as their orbits move outwards. If the orbits expand adiabatically, the scattered disc object will continue to interact with Neptune as during the main sequence. If the orbits expand non-adiabatically, then the scattered disc objects' eccentricity will change and may no longer interact with Neptune. However, the semimajor axis of a scattered disc object which is high enough to cause non-adiabatic evolution is generally too high ( $a > 10^3$  au) to remain in that population. Therefore, the scattered disc population will be subject to adiabatic mass-loss evolution and continue to interact by diffusing chaotically in semimajor axis (Yabushita 1980), likely helping to repopulate the Oort Cloud.

Beyond the scattered disc resides the Oort Cloud, which was originally postulated to contain  $\sim 10^{11}$  comets of observable size with  $5 \times 10^4 < a < 1.5 \times 10^5$  au,  $0 < e < 1$  and isotropically distributed inclinations (Oort 1950). Some of these comets occasionally

enter the inner Solar system and can achieve perihelia of a few au. These intruders are thought to have been jostled inwards by forces external to the Solar system. Many subsequent investigations since this seminal work have refined this basic picture for the outermost region of the Solar system.

The external perturbations may arise from passing stars and/or the local Galactic tide. Heisler & Tremaine (1986) demonstrated that tides likely dominate injection events into the inner Solar system, while passing stars continuously randomize the Oort Cloud comet orbital parameter distribution (Dybczyński 2002). Morris & Muller (1986) demonstrate how Galactic forces vary the orbital angular momentum of an Oort Cloud comet during a single orbit, which, hence, may be neither an ellipse nor closed. Therefore, if a typical comet's bound orbit significantly varies from Keplerian motion due to external perturbations, the analytics in Veras et al. (2011) cannot be applied to these objects without incorporating models of those perturbations.

However, if we do treat bound Oort Cloud cometary orbits as approximately elliptical, then we can estimate the effect of stellar mass loss on the cloud. One major refinement of Oort's original model is the division of the Oort Cloud into an 'inner' and 'outer' population at  $a = 2 \times 10^4$  au (Hills 1981). This bifurcation point, which determines if a comet is observable only when it is part of a shower, is still widely utilized in modern simulations and computations. Fig. 2 indicates that this bifurcation value is a factor of 2–20 times as high as the Solar system's post-main-sequence escape boundary. Hence, comets from both populations will be susceptible to escape due to post-main-sequence mass loss. Moreover, in a seminal study, Duncan, Quinn & Tremaine (1987) approximated the inner edge of the Oort Cloud to be  $\approx 3000$  au, whereas Brasser (2008) use this same value to divide the Oort Cloud further into a third 'innermost' region. High-eccentricity bodies with semimajor axes approximately equal to this potential second bifurcation point in Oort Cloud structure may be susceptible to escape during the Sun's post-main-sequence evolution if  $\eta_{\odot} < 0.6$  (see Fig. 2).

Many modern Oort Cloud investigations focus on formation and/or the orbital properties of observed comets instead of topics more relevant to this study, such as the eccentricity distribution of the vast majority of the remaining (currently unobservable) comets and the future evolution of the Oort Cloud over the next several Gyr. However, some authors (Emel'Yanenko, Asher & Bailey 2007; Brasser, Higuchi & Kaib 2010) present plots which illustrate that the eccentricity distribution of Oort Cloud comets does span from 0 to 1, with the minimum eccentricity typically increasing as  $a$  decreases. Therefore, the orbits studied in Sections 3.6.2 and 3.6.3 represent plausible families of 'inner' Oort Cloud orbits, and the orbits presented in Section 3.6.4 represent a plausible family of 'outer' Oort Cloud orbits.

Multiple subpopulations of the Oort Cloud help categorize recent discoveries. Sedna (Brown, Trujillo & Rabinowitz 2004), the most distant Solar system object yet observed (at 90.32 au), highlights the failure of the traditional scattered disc and Oort Cloud to partition the Solar system beyond the Kuiper Belt. With  $q \approx 76$  au and  $a \approx 480$  au, Sedna does not fit inside either population and demonstrates that the orbital parameter phase space of trans-Neptunian objects is larger than previously thought. If Sedna maintains its orbit until the Sun turns off the main sequence, then the object is guaranteed to remain bound (Fig. 2) during post-main-sequence mass loss, regardless of its position along its orbit. However, other objects a few hundred au more distant might not survive. Two other objects which defy easy classification are 2006 SQ<sub>372</sub> (Kaib et al. 2009), with  $q \approx 24$  au and  $a \approx 796$  au, and 2000 OO<sub>67</sub> (Veillet, Doressoundiram &

Marsden 2001; Millis et al. 2002), with  $q \approx 21$  au and  $a \approx 552$  au. The perihelia and aphelia of both objects imply that they can be classified as either scattered disc objects or Oort Cloud comets. Regardless, the short stability time-scale ( $\sim 200$  Myr) predicted for 2006 SQ<sub>372</sub> implies that it will not survive the Sun's main-sequence phase. 2000 OO<sub>67</sub> will remain bound (Fig. 2) to the post-main-sequence Sun if the object survives the Sun's main sequence.

## 4.2 Depletion characteristics

Although determining the fraction of the Oort Cloud which is depleted likely requires detailed modelling and extensive  $N$ -body simulations, we can provide some estimates here. We perform an additional three sets of simulations, for  $\eta_{\odot} = 0.2, 0.5$  and  $0.8$ , and focus on the region beyond  $10^4$  au, where most Oort Cloud objects are thought to reside. These values of  $\eta_{\odot}$  represent, in a sense, one nominal and two extreme solar evolutionary tracks. For each  $\eta_{\odot}$ , we integrate with exactly the same conditions as described in Section 3.3, but now sample 72 uniformly spaced values of  $f_0$  (for 0.5 resolution), nine uniformly spaced values of  $e_0$  in the range [0.1–0.9] and the following six values of  $a_0/\text{au} = 1.0 \times 10^4, 2.5 \times 10^4, 5.0 \times 10^4, 7.5 \times 10^4, 1.0 \times 10^5$  and  $1.25 \times 10^5$ .

The results of these simulations are presented in Figs 10–11: Fig. 10 is a cartoon which illustrates the relation between instability and initial conditions, and Fig. 11 plots the fraction of the Oort Cloud lost depending on the solar evolutionary model adopted. The cartoon indicates unstable systems with red crosses, as a function of  $a_0$ ,  $e_0$  and  $f_0$ . The connection of these variables with instability helps describe the character of the mass loss. For example, the initial conditions which lead to instability for the  $\eta_{\odot} = 0.2$  simulations (upper panel of Fig. 10) are patterned and focused towards the pericentre for higher  $a_0$  and  $e_0$  values, mimicking runaway regime behaviour and implying large mass-loss rates (see Fig. 5). In contrast, the initial conditions which lead to instability for the  $\eta_{\odot} = 0.5$  simulations (middle panel of Fig. 10) exhibit little order, implying that the mass-loss rates are not large enough to reside fully in the runaway regime, but are large enough to allow for escape. The  $\eta_{\odot} = 0.8$  simulations (lower panel of Fig. 10) provide a third alternative, showing a greater sensitivity to  $a_0$  than to either  $e_0$  or  $f_0$ . The bottom two panels indicate the difficulty in predicting the prospects for escape amidst non-linear mass loss without appealing to  $N$ -body simulations.

There are other features of Fig. 10 worth noting. Not shown are objects with  $e_0 \leq 0.2$ , because all remain stable. This implies that in no case does the Sun lose enough mass for a long enough period of time to eject distant circular bodies. In the upper panel, at least one object for every other  $(a_0, e_0)$  pair becomes unstable. Also, in this panel, asymmetric signatures about the pericentre indicate that of the two bodies at equal angular separations from pericentre, the body approaching pericentre is more likely to escape. This asymmetry does not arise in the analytic linear theory (Veras et al. 2011), but may be guessed based on physical grounds, as a planet initially approaching pericentre is more likely to be ejected than a planet initially approaching apocentre. This tendency is also suggested in Fig. 9 with the top two curves in each panel. In the bottom-rightmost ellipse in the upper panel of Fig. 10, we superimposed two brown diamonds at the locations of  $f_{\text{crit}}$  and  $360^\circ - f_{\text{crit}}$  in order to determine how closely the escape boundaries mimic the analytic boundaries which ensure that a body's eccentricity must initially decrease.

The middle and bottom panels of Fig. 10 indicate that the fraction of bodies which escape does not necessarily scale with  $a_0$ ;

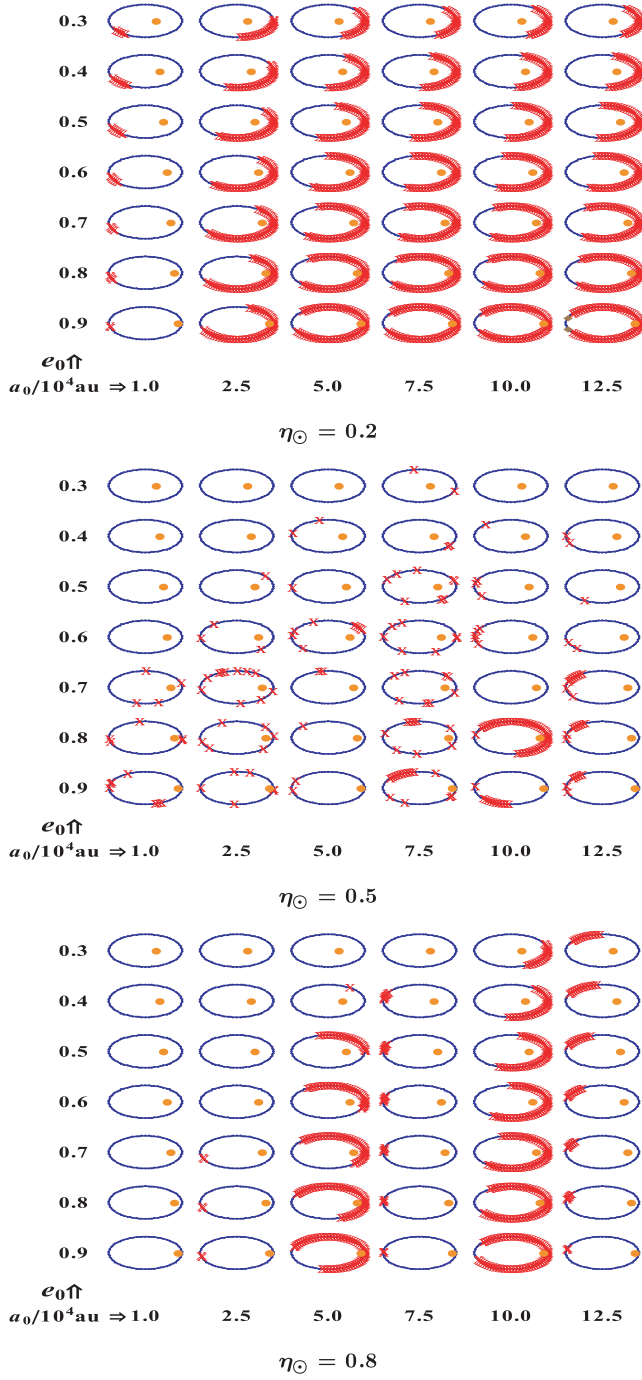


**Figure 10.** Initial condition stability snapshot for  $\eta_{\odot} = 0.2$  (upper panel),  $\eta_{\odot} = 0.5$  (middle panel) and  $\eta_{\odot} = 0.8$  (lower panel). Each scaled ellipse is for a given triplet  $(\eta_{\odot}, a_0, e_0)$  and graphically represents the initial  $f_0$  of unstable systems (large red crosses). The orange dot is a representation of the Sun, and the brown diamonds (at  $\eta_{\odot} = 0.2$  and the highest values of  $a_0$  and  $e_0$ ) represent the values  $f_{\text{crit}} = 180^\circ - (1/2)\cos^{-1}(7/9) \approx 160^\circ$  and  $360^\circ - f_{\text{crit}} \approx 200^\circ$ , which, for runaway mass loss, bound the region in which the eccentricity must initially decrease. For  $\eta_{\odot} = 0.2$ , strong 'runaway' mass loss causes objects which are closest to pericentre to be lost more easily; the effect is enhanced for higher  $a_0$  and  $e_0$ . For  $\eta_{\odot} = 0.5$ , the transitional regime between adiabatic and runaway dominates, and objects appear to go unstable at a variety of non-consecutive values of  $f_0$ . For  $\eta_{\odot} = 0.8$ , the instability appears to be highly sensitive to  $a_0$ .

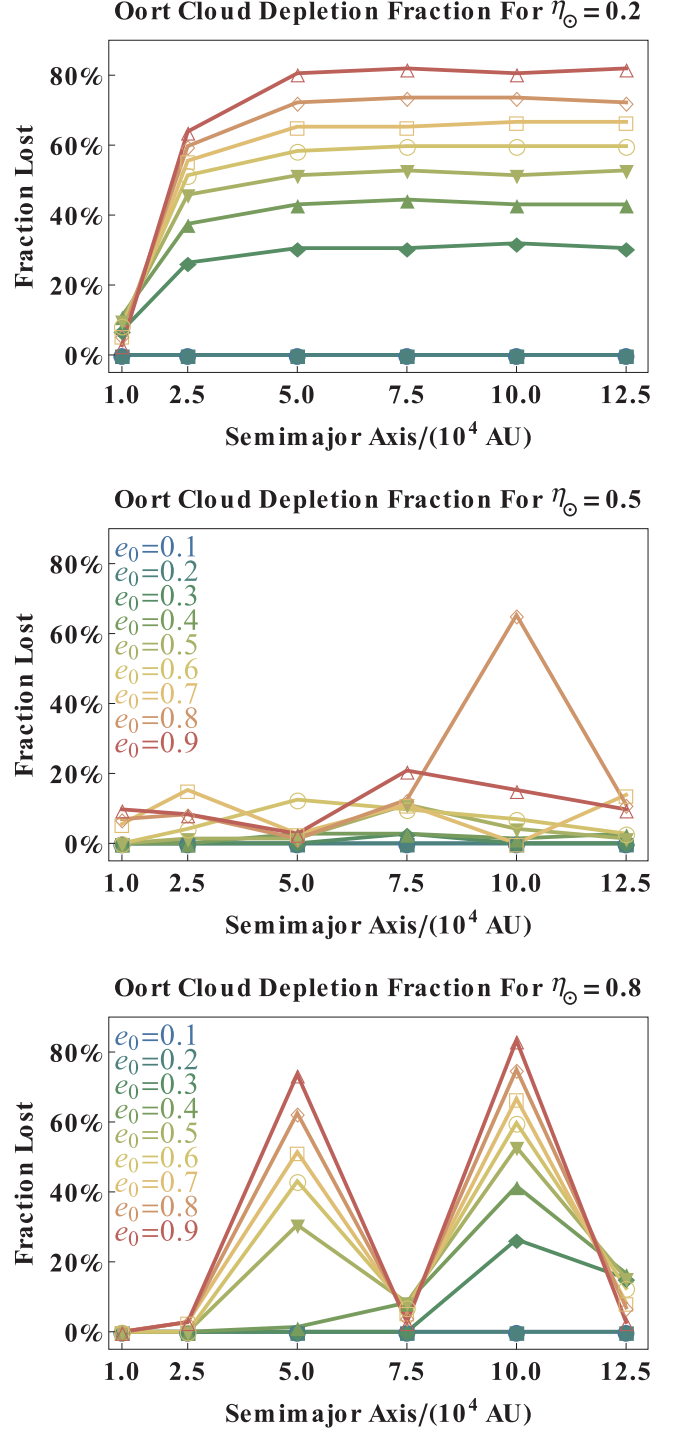


**Figure 11.** Fraction of objects which escape from the Sun for  $\eta_{\odot} = 0.2$  (top panel),  $\eta_{\odot} = 0.5$  (middle panel) and  $\eta_{\odot} = 0.8$  (bottom panel) for the simulations described in Section 4.2 and shown in Fig. 10. The  $e = 0.9, 0.8, 0.7, 0.6, 0.5, 0.4$  and  $0.3$  curves are given by the coloured curves with open triangles, open diamonds, open squares, open circles, downward filled triangles, upward filled triangles and filled diamonds, respectively. Other curves do not deviate from 0 per cent. Note the stark difference in all three distributions, demonstrating the sensitivity of Oort Cloud depletion to both the solar evolutionary model and Oort Cloud model adopted.

the bottom panel displays a dramatic double-peaked red-cross-dominated structure at  $a_0 = 5 \times 10^4$  and  $1 \times 10^5$  au. One can glean understanding of those panels by noting three points. First, the orbital periods of objects in both panels are roughly equal to the mass-loss time-scales achieved for those solar evolutionary tracks, placing the objects in a transitional regime. Secondly, the rate of change of eccentricity, which is proportional to  $(e + \cos f)$  (see Veras et al. 2011), can assume either positive or negative values *and increase or decrease* depending on the value of  $a_0$  in this transitional regime. This result is not exclusive to non-linear mass-loss prescriptions; one can show that even for a linear mass-loss rate, the inflection point of the eccentricity with respect to time contains multiple extrema in the transitional regime. Thirdly, the moment when the Sun becomes a white dwarf and stops losing mass it freezes an object's orbit, even if the orbit was approaching  $e \rightarrow 1$ . Therefore, if the  $\eta_{\odot} = 0.8$  post-main-sequence mass loss lasted longer, the distribution of unstable systems in the bottom panel would no longer be bimodal.

Fig. 11 simply counts the unstable systems from Fig. 10, and both figures can be compared directly side by side. In the top panel of Fig. 11, over 80 per cent of the highest eccentricity objects escape, and over half of all objects with  $e_0 = 0.5$  escape. The escape fractions become nearly flat for  $a \geq 5 \times 10^4$  au. In contrast, in the middle panel, all  $e_0$  curves except one maintain escape fractions which are  $<20$  per cent for all values of  $a_0$  that were sampled. In the bottom panel, the escape fractions spike at both  $a_0 = 5 \times 10^4$  and  $1 \times 10^5$  au for the five highest eccentricity curves. The results indicate how sensitive Oort Cloud depletion is to both the Oort Cloud model adopted and the solar evolution model adopted.

## 5 DISCUSSION

### 5.1 Planetary perturbations

Perturbations from surviving planets which reside within a few tens of au of the Sun will have no effect on the orbits described here, unless an external force is evoked, or one or more of the planets is ejected from the system and achieves a close encounter on its way out. As shown in Veras et al. (2011), the pericentre of an orbiting isolated body experiencing isotropic mass loss *cannot decrease*. This holds true in both the adiabatic and runaway regimes, for any mass-loss prescription. Therefore, mass loss cannot lower the pericentre of an Oort Cloud comet which was originally beyond Neptune's orbit.

How the known surviving planets evolve themselves under their mutual gravitational attraction amidst post-main-sequence mass loss is less clear. With no mass loss, the giant planets are stable until the Sun turns off the main sequence (Laskar 2008); Kholshevnikov & Kuznetsov (2011) indicate that Jupiter and Saturn need to be about 20 times more massive than their current values in order to suffer close encounters. However, Duncan & Lissauer (1998) demonstrate that with post-main-sequence mass loss, giant planet evolution may not be quiescent. In one linear mass-loss approximation, they find that Uranus and Neptune's orbits will eventually cross. More generally, if the planets remain in orbits under  $\sim 100$  au and beyond the Sun's expanding envelope, they will evolve in the adiabatic regime, expanding their near-circular orbits all at the same rate. They will remain bound according to Fig. 2. However, as multiple planets expand their orbits and maintain their relative separations, the critical separations at which the planets will remain stable will vary (Debes & Sigurdsson 2002). Also, as alluded to in Section 1, Jupiter and Saturn are predicted to largely maintain their current

orbits until the Sun turns off the main sequence. If this is true, then they will still be close to the 5:2 mean motion commensurability when significant stellar mass loss commences. How near-resonance behaviour is linked to a potentially varying critical separation is not yet clear, and suggests that much is yet to be discovered about post-main-sequence planetary systems with multiple planets.

### 5.2 Beyond the solar white dwarf

After the Sun has become a white dwarf, surviving object orbits will retain the orbital parameters achieved at the moment the Sun stopped losing mass. These objects will forever remain on these orbits unless subjected to additional perturbations. For the surviving planets, the primary perturbations will come from one another, which could lead to instabilities on Gyr, or longer, time-scales (see e.g. fig. 29 of Chatterjee et al. 2008). For objects further afield, the dominant perturbations will be external, and come from, for example, Galactic tides (e.g. Tremaine 1993)<sup>1</sup> and passing stars (e.g. Veras et al. 2009). These perturbative sources will likely play a larger role post-main sequence than during the main sequence because of orbital expansion due to mass loss. These effects may eventually unbind the object.

We define  $a_{\text{ext}}$  to be the minimum semimajor axis at which an external perturbation will eventually (at some arbitrary future time) remove an orbiting object. The brown dashed curve in Fig. 3 indicates that the Sun will lose  $\approx 48$  per cent of its current mass. Therefore, an object currently with a semimajor axis of  $a_0 \geq 0.52a_{\text{ext}}$  evolving adiabatically during post-main-sequence solar mass loss will eventually be subject to escape from these perturbations. However, if the object is in the runaway or transitional regime, then  $a_0$  will increase by a greater amount. For example, the red body in the left-hand panel of Fig. 8 increases its semimajor axis by two orders of magnitude. In the idealized case of linear mass loss for a purely runaway object on a circular orbit at apocentre, equation (44) of Veras et al. (2011) gives  $a_0 = 0.08a_{\text{ext}}$  assuming that the Sun loses 48 per cent of its mass entirely non-adiabatically in the runaway regime.

### 5.3 Exoplanet analogues

Although stellar evolutionary tracks are highly dependent on the zero-age main-sequence mass and metallicity of a star, generally the maximum value of  $\alpha$  increases as the stellar mass increases. Therefore, for stars of approximately solar metallicity which are more massive than the Sun,  $a_{\text{crit}}$  is expected to be lower than for the Solar system, and orbiting exobodies would be more prone to escape. The methodology in this work can be applied to any extrasolar system for which a stellar evolutionary track can be estimated. Given recent detections of objects which may be orbiting parent stars at  $a > 10^3$  au (Béjar et al. 2008; Leggett et al. 2008; Lafrenière et al. 2011), this type of analysis may become increasingly relevant.

## 6 CONCLUSION

The Solar system's critical semimajor axis within which bodies are guaranteed to remain bound to the dying Sun during isotropic

<sup>1</sup> Which scales as  $M_{\star}(t)^{-2/3}$  (Tremaine 1993) and might harbour an entirely different functional form from the present-day prescription due to the collision of the Milky Way and Andromeda before the Sun turns off the main sequence (Cox & Loeb 2008).

post-main-sequence mass loss and in the absence of additional perturbations is  $\approx 10^3$ – $10^4$  au. A more precise value can be obtained for a given solar evolution model; this range encompasses many realistic evolutionary tracks. The most important solar evolutionary phase for dynamical ejection may be the RGB ( $\eta_{\odot} \geq 0.7$ ), the thermally pulsing AGB ( $\eta_{\odot} \leq 0.5$ ) or the early AGB ( $0.5 \leq \eta_{\odot} < 0.7$ ). Objects with  $a \gg a_{\text{crit}}$ , such as Oort Cloud comets, and those with  $a \gtrsim a_{\text{crit}}$ , such as some scattered disc objects, may escape depending on their orbital architectures and position along their orbits. Quantifying the fraction of the population of these objects which escape would require detailed modelling of their (unknown) orbital parameters at the start of the Sun's post-main-sequence lifetime.

## ACKNOWLEDGMENT

We thank Klaus-Peter Schröder for a valuable review of this work.

## REFERENCES

- Alcock C., Fristrom C. C., Siegelman R., 1986, *ApJ*, 302, 462  
 Batygin K., Laughlin G., 2008, *ApJ*, 683, 1207  
 Béjar V. J. S., Zapatero Osorio M. R., Pérez-Garrido A., Álvarez C., Martín E. L., Rebolo R., Villalobos J., Díaz-Sánchez A., 2008, *ApJ*, 673, L185  
 Bonsor A., Wyatt M., 2010, *MNRAS*, 409, 1631  
 Brasser R., 2008, *A&A*, 492, 251  
 Brasser R., Higuchi A., Kaib N., 2010, *A&A*, 516, A72  
 Brown M. E., Trujillo C., Rabinowitz D., 2004, *ApJ*, 617, 645  
 Chambers J. E., 1999, *MNRAS*, 304, 793  
 Chatterjee S., Ford E. B., Matsumura S., Rasio F. A., 2008, *ApJ*, 686, 580  
 Cohen O., 2011, *MNRAS*, 417, 2592  
 Cox T. J., Loeb A., 2008, *MNRAS*, 386, 461  
 Debes J. H., Sigurdsson S., 2002, *ApJ*, 572, 556  
 Duncan M. J., Levison H. F., 1997, *Sci*, 276, 1670  
 Duncan M. J., Lissauer J. J., 1998, *Icarus*, 134, 303  
 Duncan M., Quinn T., Tremaine S., 1987, *AJ*, 94, 1330  
 Dybczyński P. A., 2002, *A&A*, 396, 283  
 Emel'yanenko V. V., Asher D. J., Bailey M. E., 2007, *MNRAS*, 381, 779  
 Gladman B., Chan C., 2006, *ApJ*, 643, L135  
 Gomes R. S., Fernández J. A., Gallardo T., Brunini A., 2008, *The Solar System Beyond Neptune*. Univ. Arizona Press, Tucson, p. 259  
 Hayes W. B., 2007, *Nat. Phys.*, 3, 689  
 Hayes W. B., 2008, *MNRAS*, 386, 295  
 Hayes W. B., Malykh A. V., Danforth C. M., 2010, *MNRAS*, 407, 1859  
 Heisler J., Tremaine S., 1986, *Icarus*, 65, 13  
 Hills J. G., 1981, *AJ*, 86, 1730  
 Hurley J. R., Pols O. R., Tout C. A., 2000, *MNRAS*, 315, 543  
 Iorio L., 2011, *Celest. Mech. Dynamical Astron.*, 112, 117  
 Kaib N. A., Quinn T., 2008, *Icarus*, 197, 221  
 Kaib N. A. et al., 2009, *ApJ*, 695, 268  
 Kholshevnikov K. V., Kuznetsov E. D., 2007, *Sol. Syst. Res.*, 41, 265  
 Kholshevnikov K. V., Kuznetsov E. D., 2011, *Celest. Mech. Dynamical Astron.*, 109, 201  
 Kudritzki R. P., Reimers D., 1978, *A&A*, 70, 227  
 Lafrenière D., Jayawardhana R., Janson M., Helling C., Witte S., Hauschildt P., 2011, *ApJ*, 730, 42  
 Laskar J., 2008, *Icarus*, 196, 1  
 Laskar J., Gastineau M., Delisle J.-B., Farrés A., Fienga A., 2011, *A&A*, 532, L4  
 Leggett S. K. et al., 2008, *ApJ*, 682, 1256  
 Levison H. F., Morbidelli A., Dones L., 2004, *AJ*, 128, 2553  
 Levison H. F., Morbidelli A., Vokrouhlický D., Bottke W. F., 2008, *AJ*, 136, 1079  
 Luu J., Marsden B. G., Jewitt D., Trujillo C. A., Hergenrother C. W., Chen J., Offutt W. B., 1997, *Nat*, 387, 573  
 Millis R. L. et al., 2002, *BAAS*, 34, 848  
 Morris D. E., Muller R. A., 1986, *Icarus*, 65, 1  
 Oort J. H., 1950, *Bull. Astron. Inst. Netherlands*, 11, 91  
 Parriott J., Alcock C., 1998, *ApJ*, 501, 357  
 Pitjeva E. V., Pitjev N. P., 2012, *Sol. Syst. Res.*, 46, 78  
 Sackmann I.-J., Boothroyd A. I., Kraemer K. E., 1993, *ApJ*, 418, 457  
 Schröder K.-P., Connon Smith R., 2008, *MNRAS*, 386, 155  
 Schröder K.-P., Cuntz M., 2005, *ApJ*, 630, L73  
 Sheppard S. S., 2010, *AJ*, 139, 1394  
 Tiscareno M. S., Malhotra R., 2003, *AJ*, 126, 3122  
 Tremaine S., 1993, *Planets Around Pulsars*, 36, 335  
 Vassiliadis E., Wood P. R., 1993, *ApJ*, 413, 641  
 Veillet C., Doressoundiram A., Marsden B. G., 2001, *Minor Planet Electron. Circ.*, 43  
 Veras D., Tout C. A., 2012, *MNRAS*, in press (arXiv:1202.3139)  
 Veras D., Crepp J. R., Ford E. B., 2009, *ApJ*, 696, 1600  
 Veras D., Wyatt M. C., Mustill A. J., Bonsor A., Eldridge J. J., 2011, *MNRAS*, 417, 2104  
 Volk K., Malhotra R., 2008, *ApJ*, 687, 714  
 Wood B. E., Müller H.-R., Zank G. P., Linsky J. L., 2002, *ApJ*, 574, 412  
 Yabushita S., 1980, *MNRAS*, 190, 71  
 Zendejas J., Segura A., Raga A. C., 2010, *Icarus*, 210, 539

This paper has been typeset from a TeX/LaTeX file prepared by the author.